

# Nonhierarchical Heterostructured Fe<sub>2</sub>O<sub>3</sub>/Mn<sub>2</sub>O<sub>3</sub> Porous Hollow Spheres for Enhanced Lithium Storage

Wenhao Ren, Dongna Liu, Congli Sun, Xuhui Yao, Jian Tan, Chongmin Wang,\*  
Kangning Zhao, Xuanpeng Wang, Qi Li,\* and Liqiang Mai\*

High capacity transition-metal oxides play significant roles as battery anodes benefiting from their tunable redox chemistry, low cost, and environmental friendliness. However, the application of these conversion-type electrodes is hampered by inherent large volume variation and poor kinetics. Here, a binary metal oxide prototype, denoted as nonhierarchical heterostructured Fe<sub>2</sub>O<sub>3</sub>/Mn<sub>2</sub>O<sub>3</sub> porous hollow spheres, is proposed through a one-pot self-assembly method. Beyond conventional heteromaterial, Fe<sub>2</sub>O<sub>3</sub>/Mn<sub>2</sub>O<sub>3</sub> based on the interface of (104)<sub>Fe<sub>2</sub>O<sub>3</sub></sub> and (222)<sub>Mn<sub>2</sub>O<sub>3</sub></sub> exhibits the nonhierarchical configuration, where nanosized building blocks are integrated into microsized spheres, leading to the enhanced structural stability and boosted reaction kinetics. With this design, the Fe<sub>2</sub>O<sub>3</sub>/Mn<sub>2</sub>O<sub>3</sub> anode shows a high reversible capacity of 1075 mA h g<sup>-1</sup> at 0.5 A g<sup>-1</sup>, an outstanding rate capability of 638 mA h g<sup>-1</sup> at 8 A g<sup>-1</sup>, and an excellent cyclability with a capacity retention of 89.3% after 600 cycles.

and nontoxicity, transition metal oxides (TMOs) especially Fe or Mn based materials with specific capacities (six-electron transfer reaction) ≈3 times that of graphite have gained particular attention. However, these high capacity anodes are known to suffer from severe structural degradation, unstable solid electrolyte interphase (SEI), and sluggish kinetics associated with the large volume change during lithiation/delithiation.<sup>[3]</sup> To tackle the above issues, exploring a multifunctional prototype is a straightforward way.

Heterostructures have been intensively studied as the preferable design in electrochemistry-related technologies, which provide synergetic physico-chemical properties of each pure component.<sup>[4]</sup> Such synergistic effects originating from the ionic/electronic

## 1. Introduction

The current lithium-ion battery (LIB) technology is known to reach its limit in energy density, which is largely restricted by the low capacity commercial graphite (≈372 mA h g<sup>-1</sup>).<sup>[1]</sup> Therefore, a series of high capacity anode materials including metal oxides/sulfides, alloys, phosphides, and Si compounds have been extensively studied as the alternative substitutes.<sup>[2]</sup> Considering the low cost, rich redox chemistry, tunable energy density,


transport at the solid–solid heterojunction are particularly significant for electrode construction, leading to a mild stepwise lithiation/delithiation processes with enhanced kinetics. Our group designed and synthesized 3D hierarchical MnMoO<sub>4</sub>/CoMoO<sub>4</sub> nanowires, and successfully activated the reaction sites of metal oxides, which exhibited the enhanced capacitance.<sup>[5]</sup> Gu et al.<sup>[6]</sup> reported a branched heterocomposite with β-MnO<sub>2</sub> nanorods as the backbone and porous α-Fe<sub>2</sub>O<sub>3</sub> nanorods as the branches, which displayed greatly improved rate performance and cycling reversibility. However, these heterostructures normally exhibit hierarchical characteristics due to the anisotropic crystal growth modes and the inherent lattice mismatch of each nanocrystal, resulting in limited heterojunction and partially separated components.<sup>[7]</sup>

Beyond conventional design, nonhierarchical heteromaterials based on the full coupling of each component potentially possess all-round synergistic effect of both structure and component, enabling it a finely engineered candidate with new and intriguing functionalities.<sup>[8]</sup> Furthermore, porous hollow configuration brings various benefits to electrode materials in virtue of the high porosity and internal void space, which is favorable to self-adaptive behavior and spontaneous volume expansion/contraction during lithiation/delithiation.<sup>[9]</sup> The introduction of porous hollow configuration to nonhierarchical heterostructure will likely endow the architecture with enhanced reversibility and kinetics, and thus become a superior prototype for LIB systems with large volume change. Unfortunately, few efforts so far have overcome the anisotropic crystal growth and lattice mismatch of multi-component compound, and hence the construction of nonhierarchical heterostructured TMOs is still a substantial challenge that remains to be explored.

Dr. W. Ren, D. Liu, X. Yao, J. Tan, K. Zhao, X. Wang,  
Prof. Q. Li, Prof. L. Mai  
State Key Laboratory of Advanced Technology for  
Materials Synthesis and Processing  
Wuhan University of Technology  
Wuhan 430070, China  
E-mail: qi.li@whut.edu.cn; mlq518@whut.edu.cn

Dr. W. Ren  
School of Chemistry  
Faculty of Science  
The University of New South Wales  
Sydney, New South Wales 2052, Australia

Dr. C. Sun, Prof. C. Wang  
Environmental Molecular Sciences Laboratory  
Pacific Northwest National Laboratory  
Richland, WA 99352, USA  
E-mail: chongmin.wang@pnnl.gov

 The ORCID identification number(s) for the author(s) of this article can be found under <https://doi.org/10.1002/smll.201800659>.

DOI: 10.1002/smll.201800659

Herein, we propose a one-pot self-assembly approach to exploit the nonhierarchical heterostructured porous hollow spheres (NHPHS) with the aid of  $\text{Fe}_2\text{O}_3/\text{Mn}_2\text{O}_3$  nanoparticles. As a result of this unique structure, the  $\text{Fe}_2\text{O}_3/\text{Mn}_2\text{O}_3$  achieves significant improvements in the cycling stability and rate capability for LIBs. Further structural studies followed by in situ X-ray diffraction (XRD), in situ transmission electron microscopy (TEM) characterizations, and computational analyses suggest that such a design possesses multiple functionalities: (1) The primary nanosized building blocks prevent fracture and enhance the kinetics; (2) The secondary microsized structure with relatively low surface area leads to the spatially confined SEI formation; (3) The well-defined large void space buffers the volume change and improves the stability of structure; (4) The separated redox potentials of  $\text{Fe}^{\text{III}}/\text{Fe}$  (0.9/1.8 V) and  $\text{Mn}^{\text{II}}/\text{Mn}$  (0.5/1.3 V) endow a mild stepwise volume variation process.

## 2. Results and Discussion

The NHPHS  $\text{Fe}_2\text{O}_3/\text{Mn}_2\text{O}_3$  was synthesized through a facile one-pot solvothermal method, followed by the direct heat

treatment. Schematic diagrams (Figure 1a) combined with time-dependent experiments (Figure 1b–e and Figure S1, Supporting Information) are provided to gain better insight into the evolution of the structure. At the initial stage of reaction, the pristine  $\text{FeO}_x$  nanoparticles were first formed owing to the higher binding energy of the  $\text{Fe}-\text{O}$  ( $\approx 710$  eV) versus  $\text{Mn}-\text{O}$  ( $\approx 640$  eV).<sup>[10]</sup> The chemical formula of the product is confirmed by inductively coupled plasma (ICP) analysis with the  $\text{Fe}/\text{Mn}$  atomic ratio of 957:1 (Table S1, Supporting Information). However, these nanoparticles are not thermodynamically stable over an extended period of reaction time. When the reaction is prolonged to 1 h, small  $\text{MnO}_x$  nanoparticles emerge and self-assemble with  $\text{FeO}_x$  nanoparticles to form the  $\text{Fe}_{1.44}\text{Mn}_{0.56}\text{O}_x$  half-balls (Figure 1c). Then, more binary oxide nanoparticles are involved in the self-assembly, and the well-defined hollow spheres consisted of  $\text{Fe}_{1.17}\text{Mn}_{0.83}\text{O}_x$  are obtained (Figure 1d). After calcination, the porous configuration appears on the surface of hollow spheres accompanied by the growth of original nanoparticles (Figure 1e). Notably, the oxalic acid plays an important role in controlling the pH of the solution and the hydrolytic process of metal salts. Fusiform-like nanoparticles are obtained without the addition of oxalic acid

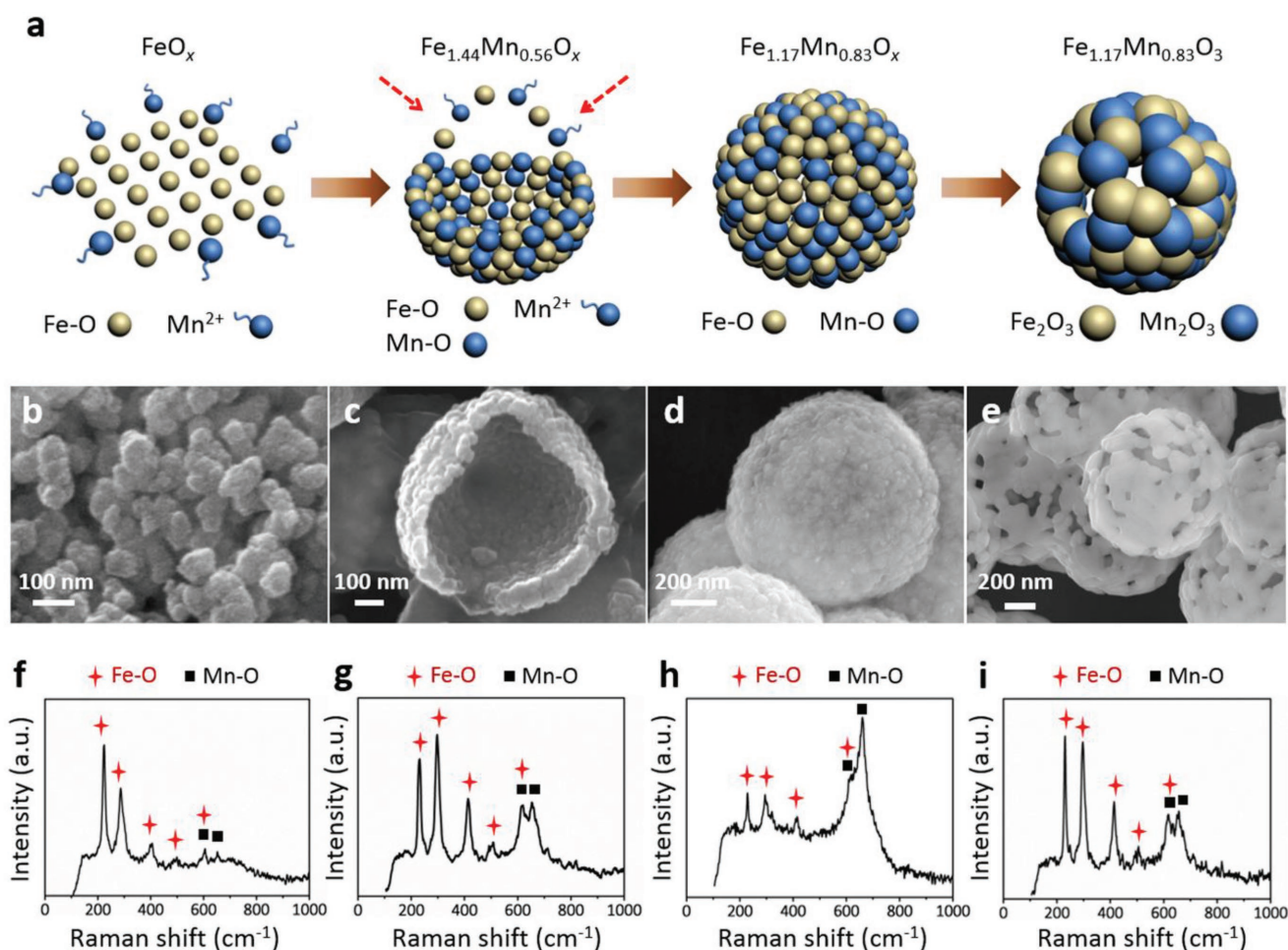


**Figure 1.** a) Schematic illustration from  $\text{FeO}_x$  nanoparticles to  $\text{Fe}_{1.44}\text{Mn}_{0.56}\text{O}_x$  half-ball, then  $\text{Fe}_{1.17}\text{Mn}_{0.83}\text{O}_x$  hollow sphere, and finally nonhierarchical heterostructured  $\text{Fe}_{1.17}\text{Mn}_{0.83}\text{O}_3$  ( $\text{Fe}_2\text{O}_3/\text{Mn}_2\text{O}_3$ ) porous hollow sphere. The FESEM images after the reaction time of b) 0.5 h, c) 1 h, d) 24 h, and e) after calcination. The corresponding Raman spectra after the reaction time of f) 0.5 h, g) 1 h, h) 24 h, and i) after calcination.

(Figure S2, Supporting Information). Ex situ Raman and Fourier transform infrared (FTIR) spectroscopy were performed to provide an in-depth understanding of the bonding evolution during this intriguing self-assembly process. As revealed by the Raman spectra (Figure 1f–i), the peaks of pristine nanoparticles are almost attributed to the Fe–O bonds ( $\text{Fe}_2\text{O}_3$ ) ranging from 200 to 600  $\text{cm}^{-1}$ .<sup>[11]</sup> Whereas, the Mn–O bonds ( $\text{Mn}_2\text{O}_3$ ) concentrated on 600–700  $\text{cm}^{-1}$  become more and more strong along with the formation of heterostructured hollow spheres,<sup>[12]</sup> which is in good agreement with ICP analysis. Notably, the peak at  $\approx 605 \text{ cm}^{-1}$  can be assigned to the vibrational modes of O–Fe/Mn–O, and it exhibits obvious Raman peak shift toward higher wavenumber region as the increase of reaction time (Figure S4, Supporting Information), which suggests that the cobonding of Fe–O–Mn emerged during the self-assembly process.<sup>[13]</sup> The O–Fe/Mn–O bonding evolution are also confirmed by the FTIR (Figure S5, Supporting Information), which can be attributed to their similar ion radius and 4d electrons status.<sup>[14]</sup> Taking these experimental results into consideration, we can deduce that the formation of porous hollow spheres relies on a cobonding induced self-assembly process with O atoms as the bridge. For comparison, the simplex  $\alpha\text{-Fe}_2\text{O}_3$  and  $\alpha\text{-Mn}_2\text{O}_3$  were also prepared with the same method except for the addition of Mn or Fe sources, respectively (Figure S6, Supporting Information).

The crystal structure of as-synthesized samples was then determined through XRD measurement, from which the NHPHS  $\text{Fe}_2\text{O}_3/\text{Mn}_2\text{O}_3$  was well indexed to the hybrid phase of  $\alpha\text{-Fe}_2\text{O}_3$  (JCPDS No. 79-0007) and  $\alpha\text{-Mn}_2\text{O}_3$  (JCPDS No. 71-0636), and no other impurities were detected (Figure 2a). Figure 2b shows the general view of the crystal structures of  $\alpha\text{-Fe}_2\text{O}_3$  and  $\alpha\text{-Mn}_2\text{O}_3$  with the exposed (104) $_{\text{Fe}_2\text{O}_3}$  and (222) $_{\text{Mn}_2\text{O}_3}$ . The morphology of the samples was investigated by the field-emission scanning electron microscopy (FESEM). It is clearly observed that heterostructured spheres are uniform in size, possessing a hollow structure with randomly distributed voids on the surface (Figure 2c). The energy-dispersive spectrometry (EDS) mappings and corresponding line scan indicate that the Fe and Mn are heterogeneously distributed in  $\text{Fe}_2\text{O}_3/\text{Mn}_2\text{O}_3$ , indicating the successful construction of nonhierarchical heterostructure without structural separation (Figure 2d–g). It is worth noting that the Brunauer–Emmett–Teller (BET) surface area of NHPHS  $\text{Fe}_2\text{O}_3/\text{Mn}_2\text{O}_3$  is relatively low (24.2  $\text{m}^2 \text{ g}^{-1}$ ), and there are two distinct pore size distributions concentrated on 2–4 and 10–80 nm (Figure S7, Supporting Information), respectively. As evidenced by the X-ray photoelectron spectroscopy (XPS, Figure S8, Supporting Information), two peaks of Mn 2p at 641.4 and 652.9 eV could be assigned to  $\text{Mn}^{\text{III}}$ , and two other peaks of Fe 2p located at 710.6 and 724.2 eV with a satellite peak at 718.9 eV could be indexed to  $\text{Fe}^{\text{III}}$ . Moreover, the phase distributions and crystal patterns were investigated through high-resolution TEM (HRTEM). Figure 2h clearly reveals that there are three distinct lattice fringes existing in the structure of  $\text{Fe}_2\text{O}_3/\text{Mn}_2\text{O}_3$ , and its corresponding fast Fourier transformation (FFT) results can be well identified as  $\text{Fe}_2\text{O}_3$  (Figure 2j),  $\text{Mn}_2\text{O}_3$  (Figure 2k), and a junction region (Figure 2l), respectively. The further examination on lattice fringes clearly confirms the plane orientations of (104) $_{\text{Fe}_2\text{O}_3}$ , (116) $_{\text{Fe}_2\text{O}_3}$ , (012) $_{\text{Fe}_2\text{O}_3}$ , (440) $_{\text{Mn}_2\text{O}_3}$ , (400) $_{\text{Mn}_2\text{O}_3}$ , and (222) $_{\text{Mn}_2\text{O}_3}$ .

Considering the major lattice fringe orientations of (104) $_{\text{Fe}_2\text{O}_3}$  and (222) $_{\text{Mn}_2\text{O}_3}$  shown in Figure 2h, the interface between  $\alpha\text{-Fe}_2\text{O}_3$  and  $\alpha\text{-Mn}_2\text{O}_3$  can be attributed to the (104) $_{\text{Fe}_2\text{O}_3}$ //(222) $_{\text{Mn}_2\text{O}_3}$ . This epitaxial growth is also supported by their crystal structures as shown in Figure 2b. The theoretical lattice mismatches between (104) $_{\text{Fe}_2\text{O}_3}$  and (222) $_{\text{Mn}_2\text{O}_3}$  are less than 1% ( $d_{(104)} = 2.70 \text{ \AA}$ ,  $d_{(222)} = 2.72 \text{ \AA}$ ), which is small enough to be tolerated for the anisotropic growth.

To evaluate the lithium storage behavior and explore the structure–property relationship, lithium batteries were fabricated based on the  $\text{Fe}_2\text{O}_3/\text{Mn}_2\text{O}_3$ ,  $\text{Fe}_2\text{O}_3$ , and  $\text{Mn}_2\text{O}_3$  electrodes. The cyclic voltammetry (CV, Figure 3a) was conducted at a voltage window of 0.01 to 3.0 V versus  $\text{Li}^+/\text{Li}$  at a scan rate of 0.1  $\text{mV s}^{-1}$ . During the first cycle, four cathodic peaks of  $\text{Fe}_2\text{O}_3/\text{Mn}_2\text{O}_3$  located at 1.15, 0.64, 0.57, and 0.42 V are detected. The initial peak (1.15 V) can be ascribed to the reduction of  $\text{Mn}^{\text{III}}$  to  $\text{Mn}^{\text{II/III}}$  ( $\text{Mn}_3\text{O}_4$ ), and the other two peaks located at 0.64 and 0.57 V can be assigned to the stepwise reduction of  $\text{Fe}^{\text{III}}$  to Fe and  $\text{Mn}^{\text{III/II}}$  to  $\text{Mn}^{\text{II}}$ , meanwhile the peak centered at 0.42 V is attributed to the complete reduction of  $\text{Mn}^{\text{II}}$  to  $\text{Mn}$ .<sup>[11b]</sup> In the subsequent anodic scan, two broad oxidation peaks at 1.33 and 1.68 V can be assigned to the oxidation of  $\text{Mn} \rightarrow \text{MnO}_x$  and  $\text{Fe} \rightarrow \text{FeO}_x$ , respectively. No peaks at above 2.2 V are observed, which means the further oxidation from  $\text{Mn}^{\text{II}}$  to  $\text{Mn}^{\text{III}}$  does not occur. For the second cycle, the lithiation voltages of  $\text{FeO}_x$  and  $\text{MnO}_x$  are improved to 0.93 and 0.53 V, whereas the intensity of peaks decreases, which corresponds to the promoted kinetics of the electrode resulting from the nanosize effect and the irreversible phase transformation with the formation of SEI.<sup>[15]</sup> CV tests of  $\text{Fe}_2\text{O}_3$  and  $\text{Mn}_2\text{O}_3$  were also conducted, which exhibit similar redox peaks in accordance with above analysis (Figure S9, Supporting Information). Figure 3b shows the galvanostatic charge–discharge curves of  $\text{Fe}_2\text{O}_3/\text{Mn}_2\text{O}_3$  for the selected cycles at a current density of 1  $\text{A g}^{-1}$ , where the voltage plateaus are in good agreement with CV results. During the extended cycles, the voltage plateaus of  $\text{Fe}_2\text{O}_3/\text{Mn}_2\text{O}_3$  demonstrate negligible hysteresis, and the capacity retention from 2nd to 100th cycles is 98.6%, indicating the excellent structural reversibility.

The rate capabilities of  $\text{Fe}_2\text{O}_3/\text{Mn}_2\text{O}_3$ ,  $\text{Fe}_2\text{O}_3$ , and  $\text{Mn}_2\text{O}_3$  electrodes were further evaluated. As shown in Figure 3c, the  $\text{Fe}_2\text{O}_3/\text{Mn}_2\text{O}_3$  exhibits a high discharge capacity of 1075  $\text{mA h g}^{-1}$  at 0.5  $\text{A g}^{-1}$ , and still maintains a substantial capacity of 638  $\text{mA h g}^{-1}$  even though the current density increases by 16 times (8.0  $\text{A g}^{-1}$ ), corresponding to 59.3% capacity retention. Notably, when the current density turns back to 0.5  $\text{A g}^{-1}$ , no capacity decay is observed compared to the initial state. The complete recovery of the capacity after extensive cycling at various currents implies that the electrode was not damaged and the integrity of the structure was maintained during cycling. The coulombic efficiency of  $\text{Fe}_2\text{O}_3/\text{Mn}_2\text{O}_3$  is stabilized at around 100% except for the current change sites throughout cycling, indicating the steady SEI formation without the particle fracture. Figure 3d displays the charge–discharge curves of  $\text{Fe}_2\text{O}_3/\text{Mn}_2\text{O}_3$  from 0.5 to 8  $\text{A g}^{-1}$ . There is no significant hysteresis increase in charge–discharge plateaus even at a high rate of 8  $\text{A g}^{-1}$ , demonstrating rapid electronic/ionic transport kinetics. The discharge capacity versus current density of  $\text{Fe}_2\text{O}_3/\text{Mn}_2\text{O}_3$ ,  $\text{Fe}_2\text{O}_3$ , and  $\text{Mn}_2\text{O}_3$  electrodes are summarized (Figure S10, Supporting Information).



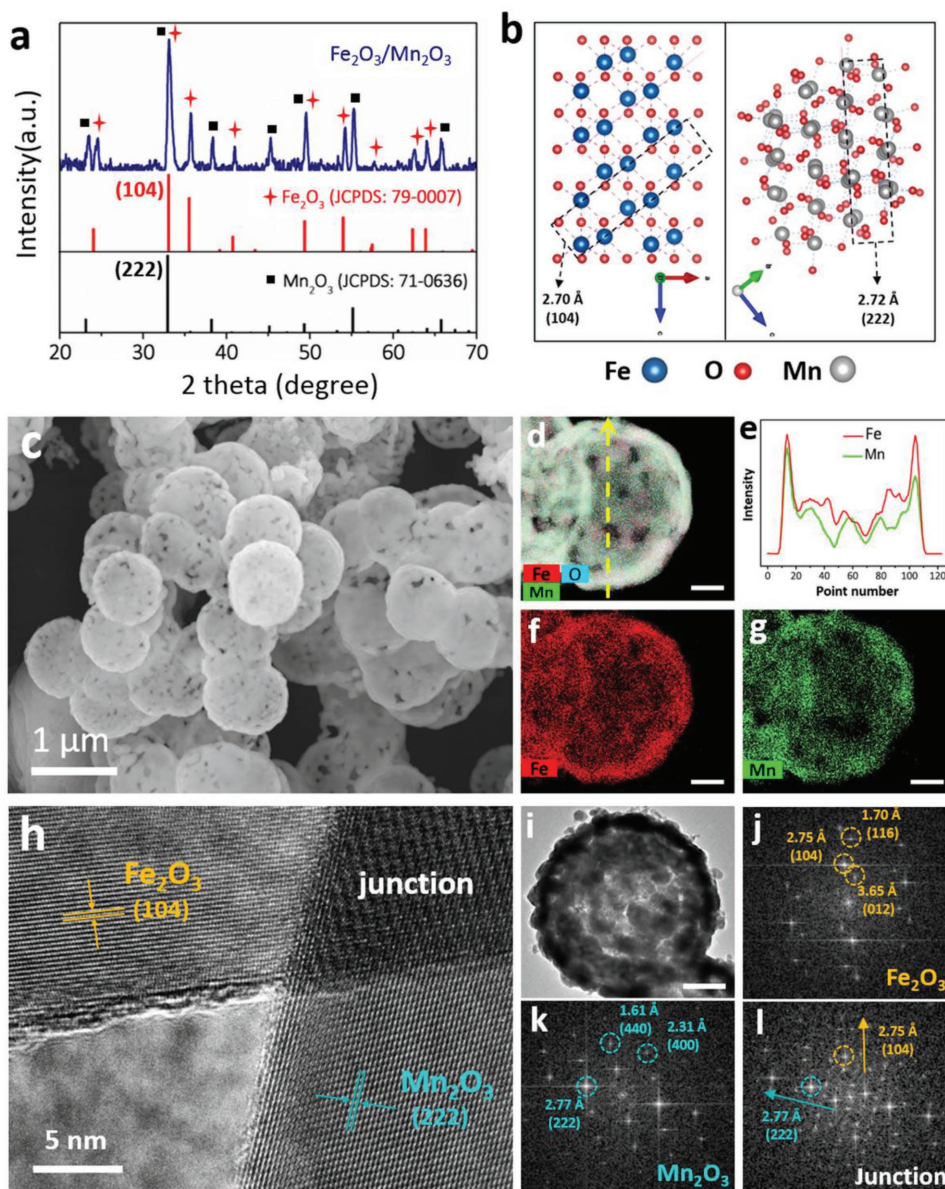


**Figure 2.** a) XRD patterns of NHPHS  $\text{Fe}_2\text{O}_3/\text{Mn}_2\text{O}_3$ . b) Crystal structures of  $\alpha\text{-Fe}_2\text{O}_3$  (left) and  $\alpha\text{-Mn}_2\text{O}_3$  (right). c) SEM image of NHPHS  $\text{Fe}_2\text{O}_3/\text{Mn}_2\text{O}_3$ . d–g) EDS mappings and corresponding line scan of the single sphere (scale bar: 200 nm). h, i) HRTEM and TEM image (scale bar: 200 nm) of  $\text{Fe}_2\text{O}_3/\text{Mn}_2\text{O}_3$ . j–l) FFT patterns derived from (h).

It is found that these three samples exhibit similar initial discharge capacities of above  $1000 \text{ mA h g}^{-1}$  at  $0.5 \text{ A g}^{-1}$ . While the capacity decay of  $\text{Fe}_2\text{O}_3/\text{Mn}_2\text{O}_3$  is much smaller than  $\text{Fe}_2\text{O}_3$  and  $\text{Mn}_2\text{O}_3$  upon further increasing the current density. When the current density reaches  $8 \text{ A g}^{-1}$ , the  $\text{Fe}_2\text{O}_3/\text{Mn}_2\text{O}_3$  exhibits a discharge capacity of  $638 \text{ mA h g}^{-1}$ , which is two to three times higher than  $\text{Fe}_2\text{O}_3$  and  $\text{Mn}_2\text{O}_3$ , suggesting the superiority of this prototype structure. The long-term structural durability of the electrodes was also investigated at  $1 \text{ A g}^{-1}$  (Figure 3e). Notably, the  $\text{Fe}_2\text{O}_3/\text{Mn}_2\text{O}_3$  displays a discharge capacity of  $954 \text{ mA h g}^{-1}$  at the second cycle. After 600 cycles, the discharge capacity still remains  $852 \text{ mA h g}^{-1}$ , corresponding to a capacity retention of 89.3% relative to the second cycle, which significantly exceeds the reversibility of

$\text{Fe}_2\text{O}_3$  (43.9%) and  $\text{Mn}_2\text{O}_3$  (7.8%). Notably, the enhanced performance of  $\text{Fe}_2\text{O}_3/\text{Mn}_2\text{O}_3$  is achieved without protective shell or carbon coating, which is supported by the Raman analysis that no existence of D or G characteristic peaks of carbon can be observed (Figure S12, Supporting Information). All these results combined with electrochemical data demonstrate that porous hollow spheres with nonhierarchical heterostructure possess both the enhanced stability and improved kinetics (Table S2, Supporting Information).

To gain deeper insight into the structural evolution of  $\text{Fe}_2\text{O}_3/\text{Mn}_2\text{O}_3$  during the lithiation and delithiation, in situ XRD measurement was performed (Figure 4a). During the initial lithiation process, no peak shift is observed, but the peak intensity is found to weaken promptly upon discharging, indicating

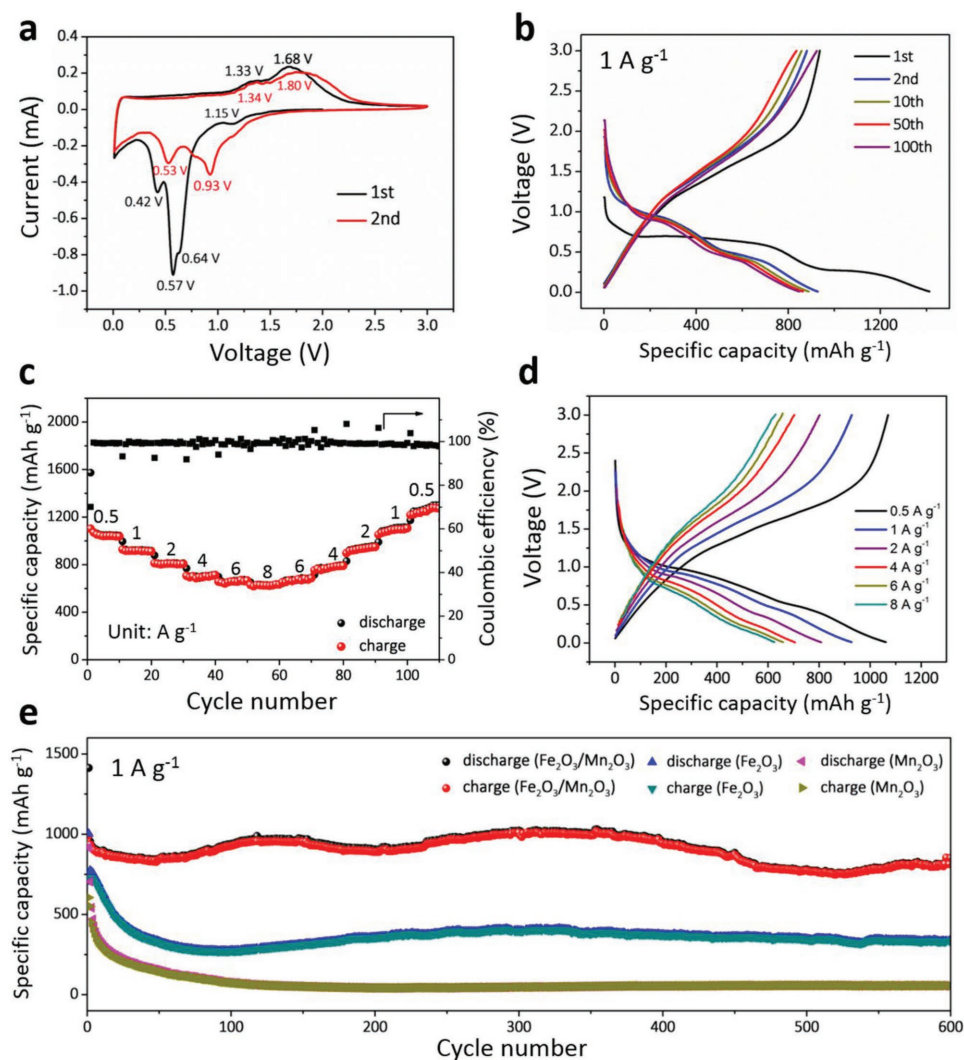


**Figure 3.** a) CV profiles of  $\text{Fe}_2\text{O}_3/\text{Mn}_2\text{O}_3$  from 0.01 to 3.0 V. b) Charge–discharge curves of  $\text{Fe}_2\text{O}_3/\text{Mn}_2\text{O}_3$  at different cycles. c,d) Rate performance and corresponding charge–discharge curves of  $\text{Fe}_2\text{O}_3/\text{Mn}_2\text{O}_3$  at different current densities of 0.5, 1, 2, 4, 6, and 8  $\text{A g}^{-1}$ . e) Long-term cycling performance of  $\text{Fe}_2\text{O}_3/\text{Mn}_2\text{O}_3$  at a current density of 1  $\text{A g}^{-1}$ .

the decomposition of pristine  $\text{Fe}_2\text{O}_3$  and  $\text{Mn}_2\text{O}_3$ . The peaks that belong to the (104) and (110) plane of  $\text{Fe}_2\text{O}_3$ , and (222) plane of  $\text{Mn}_2\text{O}_3$  disappear at about 0.8 V. No obvious diffraction peaks can be detected when the electrode is recharged from 0.01 to 3.00 V after the first cycle. The disappearance of diffraction peaks implies that there is a phase amorphization during the initial lithiation process, meanwhile, the less crystalline structure could provide more active sites and faster ion diffusion kinetics.<sup>[16]</sup> CV measurements at different scan rate were further performed to clarify the  $\text{Li}^+$  storage mechanism. Figure 4b shows two pairs of anodic/cathodic peaks arising from the fast faradaic redox reactions of  $\text{Mn} \leftrightarrow \text{MnO}_x$  and  $\text{Fe} \leftrightarrow \text{FeO}_x$ , and there are noticeable peaks shift as the sweep rate increases. Assuming that the current obeys a power-law relationship with the sweep rate, a general equation for analyzing the electrochemical kinetics processes is described as follows<sup>[17]</sup>

$$i = av^b \quad (1)$$

where  $a$  and  $b$  are adjustable values,  $i$  is the current (A) and  $v$  is the scan rate ( $\text{V s}^{-1}$ ). Whereas a  $b$ -value of 0.5 indicates that the current is controlled by semi-infinite linear diffusion, a value of 1.0 represents a surface-controlled process. Figure 4c presents a plot of  $\log(i)$  versus  $\log(v)$  from 0.1 to 1.0  $\text{mV s}^{-1}$  for both cathodic and anodic peaks. The  $b$ -value determined by the slopes of the four redox peaks are 0.90, 0.93, 0.90, and 0.95, respectively, which implies that the kinetics of  $\text{Fe}_2\text{O}_3/\text{Mn}_2\text{O}_3$  anode are surface-controlled, and thus fast.

To further clarify the solid-state diffusion kinetics of  $\text{Fe}_2\text{O}_3/\text{Mn}_2\text{O}_3$  electrode, galvanostatic intermittent titration technique (GITT) was employed, and the electrodes were first cycled at 1  $\text{A g}^{-1}$  for 50 cycles to reach the normal operation state prior to the GITT test. It is found that the  $\text{Fe}_2\text{O}_3/\text{Mn}_2\text{O}_3$  exhibits the highest discharge capacity of 1307  $\text{mA h g}^{-1}$  with the smallest hysteresis among three anodes (Figure 4d). Obviously, the overpotential of anodes displays a gradual increase during delithiation and decrease during lithiation, and their reaction



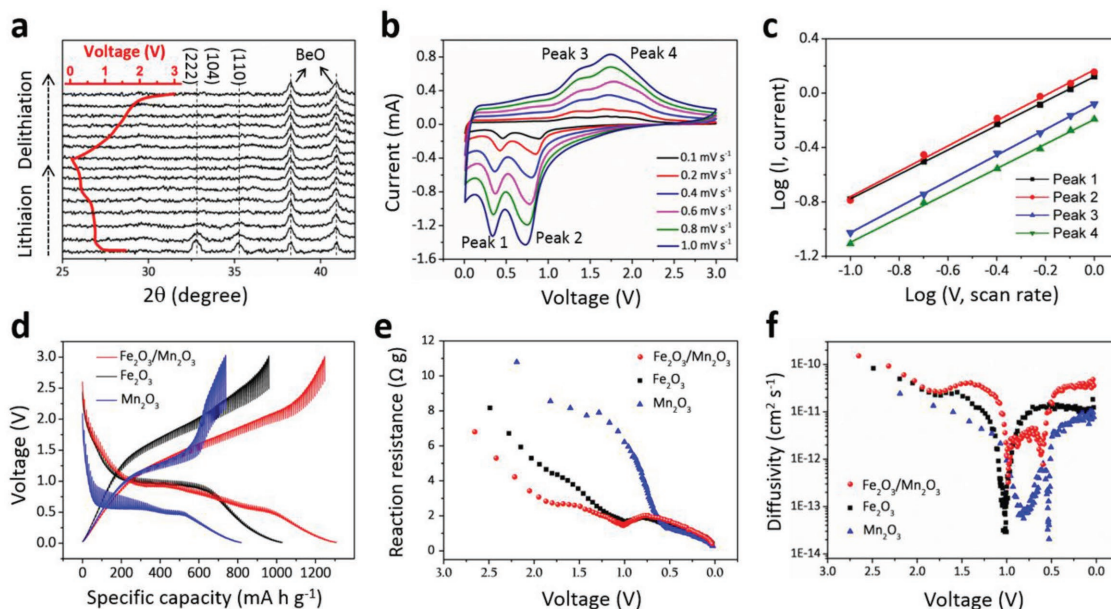


**Figure 4.** a) In situ XRD curves of  $\text{Fe}_2\text{O}_3/\text{Mn}_2\text{O}_3$  during the initial lithiation and delithiation. b) CV profiles of  $\text{Fe}_2\text{O}_3/\text{Mn}_2\text{O}_3$  at different scan rate from 0.1 to 1.0  $\text{mV s}^{-1}$ . c)  $\log(i)$  versus  $\log(v)$  plots at specific peak currents. d) The potential response, e) reaction resistance, and f) diffusivity of  $\text{Fe}_2\text{O}_3/\text{Mn}_2\text{O}_3$ ,  $\text{Fe}_2\text{O}_3$ , and  $\text{Mn}_2\text{O}_3$  derived from GITT measurement.

resistances as a function of depth-of-discharge were calculated through dividing the overpotential by the pulse current (Figure S14, Supporting Information). As depicted in Figure 4e, the  $\text{Fe}_2\text{O}_3/\text{Mn}_2\text{O}_3$  demonstrates the lowest reaction resistance compared with  $\text{Fe}_2\text{O}_3$  and  $\text{Mn}_2\text{O}_3$ , indicating the improved reaction kinetics.<sup>[18]</sup> Based on the transient voltage responses, the chemical diffusion coefficients of  $\text{Li}^+$  ( $D^{\text{GITT}}$ ) at different ion insertion status were then computationally analyzed (Figure 4f) according to the following Equation (2)<sup>[19]</sup>

$$D^{\text{GITT}} = \frac{4}{\pi\tau} \left( \frac{m_{\text{B}} V_{\text{M}}}{M_{\text{B}} S} \right)^2 \left( \frac{\Delta E_{\text{s}}}{\Delta E_{\text{T}}} \right)^2 \quad (2)$$

where  $\tau$  is the constant current pulse time,  $m_{\text{B}}$ ,  $V_{\text{M}}$ ,  $S$ , and  $M_{\text{B}}$  are the mass, molar volume, electrode–electrolyte interface area, and molar mass of the sample, respectively.  $\Delta E_{\text{s}}$  is the voltage difference during the open-circuit period, and  $\Delta E_{\text{T}}$  is the total change of cell voltage during a constant current pulse excluding the  $IR$  drop (Figure S15, Supporting Information). The calculated  $D^{\text{GITT}}$  of  $\text{Fe}_2\text{O}_3/\text{Mn}_2\text{O}_3$ ,  $\text{Fe}_2\text{O}_3$ , and  $\text{Mn}_2\text{O}_3$  electrodes are in range of  $10^{-10}$ – $10^{-13}$ ,  $10^{-10}$ – $10^{-14}$ , and  $10^{-10}$ – $10^{-14}$   $\text{cm}^2 \text{ s}^{-1}$ , respectively. A similar trend is observed for all three electrodes with a minimum diffusivity at the beginning of redox plateaus, at which the  $D^{\text{GITT}}$  of  $\text{Fe}_2\text{O}_3$  and  $\text{Mn}_2\text{O}_3$  drops rapidly to about  $10^{-14}$   $\text{cm}^2 \text{ s}^{-1}$ , indicating a sluggish electrochemical kinetics. By contrast, the  $D^{\text{GITT}}$  of  $\text{Fe}_2\text{O}_3/\text{Mn}_2\text{O}_3$  maintains at above  $10^{-13}$   $\text{cm}^2 \text{ s}^{-1}$ , which means the construction of Fe–Mn binary oxide essentially promotes the solid-state diffusion kinetics even though the BET surface area of NHPHS  $\text{Fe}_2\text{O}_3/\text{Mn}_2\text{O}_3$  is relatively low ( $24.2 \text{ m}^2 \text{ g}^{-1}$ ).

There are overall four steps of redox reactions occurring among the electrode, including the reduction of  $\text{Fe}_2\text{O}_3$  to Fe (0.9 V) and MnO to Mn (0.5 V) during the lithiation, and the corresponding reversible oxidation of Fe to  $\text{Fe}_2\text{O}_3$  (1.8 V) and

Mn to MnO (1.3 V) during the delithiation (Figure 5a). This multicomponent lithiation/delithiation redox reaction essentially ensures a mild stepwise volume expansion/contraction process. Considering the large internal free space provided by the porous hollow configuration, it is expected that the stress/strain can be well released, resulting in the stabilized structure and SEI. In situ TEM technology was utilized to directly observe the volume variation during lithiation, where NHPHS  $\text{Fe}_2\text{O}_3/\text{Mn}_2\text{O}_3$  acted as the working electrode, bulk metallic Li@Li<sub>2</sub>O as the counter electrode, and the lithiation/delithiation process was driven by an external constant voltage. The lithiation process started when Li@Li<sub>2</sub>O probe contacted with the working electrode. There is a continuous volume expansion as the lithiation proceeds, but the structure retains its integrity (Figure 5b–e). After 180 s of reaction, a limited volume expansion of 31% is observed, which can be attributed to enough internal space and multistep volume variation. Furthermore, a high-resolution lithiation procedure was also conducted to monitor the evolution of single nanoparticles (Figure S16, Supporting Information). A quick expansion of  $\text{Fe}_2\text{O}_3/\text{Mn}_2\text{O}_3$  nanoparticles is clearly detected as the reaction proceeds, while no nanoparticle pulverization occurs during the whole lithiation time, indicating the stable structure of nanosized building blocks. Ex situ SEM of NHPHS  $\text{Fe}_2\text{O}_3/\text{Mn}_2\text{O}_3$  after 50 deep cycles was then presented to study the structural change after cycling. Nearly perfect spherical microsized particles are observed with uniform and stable SEI coated on the surface (Figure 5f). After removing the SEI with ethanol through ultrasound treatment, intact porous hollow spheres clearly emerge, and the diameter of the sphere shows only 10% decrease from 1.0 to 0.9  $\mu\text{m}$  (Figure 5g). It is safe to draw the conclusion that this new heterostructure design not only accommodates the internal volume expansion but also retains the structural integrity of the secondary microsized structure with confined SEI on the surface.

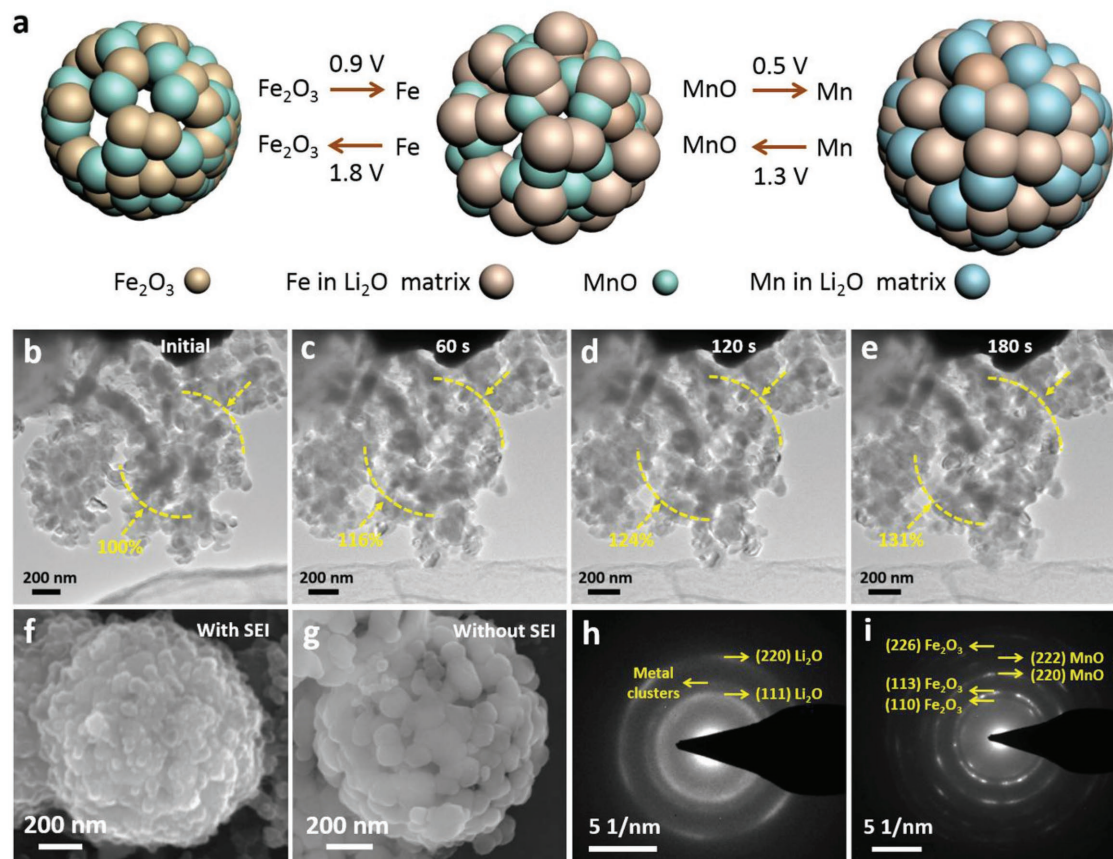
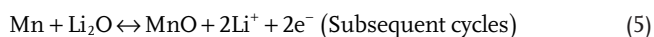
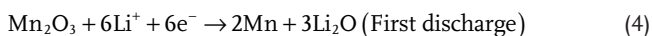
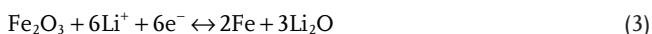


**Figure 5.** a) Schematic of the stepwise charge–discharge process of  $\text{Fe}_2\text{O}_3/\text{Mn}_2\text{O}_3$  after the first lithiation. b–e) In situ TEM images of  $\text{Fe}_2\text{O}_3/\text{Mn}_2\text{O}_3$  during lithiation process from initial state to 180 s. f, g) Typical SEM images of  $\text{Fe}_2\text{O}_3/\text{Mn}_2\text{O}_3$  after 50 cycles. SAED patterns of  $\text{Fe}_2\text{O}_3/\text{Mn}_2\text{O}_3$  after 50 cycles at h) lithiated and i) delithiated state.

The reaction mechanism of NHPHS  $\text{Fe}_2\text{O}_3/\text{Mn}_2\text{O}_3$  was investigated through the selected area electron diffraction (SAED) analysis. During the lithiation, the Li ions completely react with the  $\text{Fe}_2\text{O}_3/\text{Mn}_2\text{O}_3$  to form the metallic Fe and Mn (Figure 5h). Two distinct diffraction rings assigned to the (111) and (220) of  $\text{Li}_2\text{O}$  matrix (JCPDS No. 77-2144) are explicitly detected, while the diffraction rings of metal clusters are overlapped, in which the  $d$ -spacing is 2.08 Å, corresponding to the (110) plane of Fe (JCPDS No. 87-0722) and (310) plane of Mn (JCPDS No. 01-1234). At the delithiated state (Figure 5i), four diffraction rings are observed, and the two lattice spacings in the SAED pattern are calculated to be 2.68 and 2.18 Å, which are in good agreement with the (104) and (113) planes of  $\text{Fe}_2\text{O}_3$  (JCPDS No. 79-0007), indicating the complete redox reaction of  $\text{Fe}^{\text{III}} \leftrightarrow \text{Fe}$ . Meanwhile, the other two diffraction rings with the spacings of 1.57 and 1.27 Å can be identified as the (220) and (222) planes of MnO (JCPDS No. 78-0424), revealing the reaction mechanism of  $\text{Mn}^{\text{II}} \leftrightarrow \text{Mn}$ . The SAED analysis is in good agreement with the CV results. On the basis of above comprehensive study, the total conversion reaction mechanism of  $\text{Fe}_2\text{O}_3/\text{Mn}_2\text{O}_3$  can be summarized as follows



In short, there are two interdependent characteristics of this unique design that enable  $\text{Fe}_2\text{O}_3/\text{Mn}_2\text{O}_3$  a superior LIB anode. On the one hand, the formation of Fe–Mn binary oxides, which deliver rich redox chemistry of  $\text{Fe}^{\text{III}}/\text{Fe}$  (0.9/1.8 V) and  $\text{Mn}^{\text{II}}/\text{Mn}$  (0.5/1.3 V), resulting in a mild stepwise volume variation process. Moreover, the primary nanosized building blocks prevent fracture, and the full coupling of binary oxides provides higher  $\text{Li}^+$  diffusivity compared with simplex  $\text{Fe}_2\text{O}_3$  or  $\text{Mn}_2\text{O}_3$ . On the other hand, from the perspective of porous hollow configuration, the large free space in the hollow framework benefits to the strain–relaxation, meanwhile the porous structure is able to release the interacted stress, collectively leading to the rapid self-adaptive behavior during the structural change. Besides, the secondary microsized spheres show relatively low surface area, leading to the partially confined SEI formation.

### 3. Conclusion

Nonhierarchical heterostructured porous hollow spheres composed of  $\text{Fe}_2\text{O}_3/\text{Mn}_2\text{O}_3$  nanoparticles are constructed based on the small lattice mismatches (<1%) between (104) $_{\text{Fe}_2\text{O}_3}$  and (222) $_{\text{Mn}_2\text{O}_3}$ . With this design,  $\text{Fe}_2\text{O}_3/\text{Mn}_2\text{O}_3$  exhibits a high

discharge capacity (1075 mA h g<sup>-1</sup> at 0.5 A g<sup>-1</sup>), an outstanding rate capability (638 mA h g<sup>-1</sup> at 8.0 A g<sup>-1</sup>), as well as a superior cycling stability (89.3% after 600 cycles) as LIBs anode. Through in situ XRD/TEM as well as computational analyses, its structure–property relationship and lithium storage mechanism have been well understood, from which this unique structure is revealed to take all-round synergistic benefits of both structure and component. We believe this nonhierarchical heterostructure prototype can be extended to construct other high-capacity electrodes with enhanced electrochemical reliability, and accelerate the development of electrochemical energy storage.

## 4. Experimental Section

**Synthesis of NHPHS Fe<sub>2</sub>O<sub>3</sub>/Mn<sub>2</sub>O<sub>3</sub>:** Nonhierarchical heterostructured porous hollow spheres, made up of Fe<sub>1.17</sub>Mn<sub>0.83</sub>O<sub>3</sub>, were synthesized via a one-pot self-assembly solvothermal method followed by a direct heat treatment. First, 1 mmol Fe(NO<sub>3</sub>)<sub>3</sub>·9H<sub>2</sub>O, 1 mmol Mn(CH<sub>3</sub>COO)<sub>2</sub>·4H<sub>2</sub>O, and 3 mmol H<sub>2</sub>C<sub>2</sub>O<sub>4</sub>·2H<sub>2</sub>O were dissolved into 35 mL of *N,N*-dimethylformamide (DMF) with stirring for 0.5 h at 70 °C in water bath. The obtained wine-red solution was transferred into 50 mL Teflon-lined autoclave and kept at 200 °C for 24 h, then cooled down to room temperature naturally. The as-obtained products were collected and washed with distilled water and ethanol for several times, and dried at 70 °C overnight. In the end, the product was obtained from the precursor via preheating it at 400 °C for 5 h followed by annealing at 650 °C for 10 h with a heating rate of 5 °C min<sup>-1</sup>. For comparison, the simplex Fe<sub>2</sub>O<sub>3</sub> and Mn<sub>2</sub>O<sub>3</sub> samples were also synthesized with the same method except for the addition of Mn(CH<sub>3</sub>COO)<sub>2</sub>·4H<sub>2</sub>O or Fe(NO<sub>3</sub>)<sub>3</sub>·9H<sub>2</sub>O, respectively.

**Characterization:** XRD measurement was performed to investigate the crystallographic information using a D8 Advance X-ray diffractometer with Cu K $\alpha$  X-ray source. BET surface areas were measured using Tristar II 3020 instrument by nitrogen adsorption at 77 K. Raman spectra were obtained using a Renishaw INVIA micro-Raman spectroscopy system. FTIR transmittance spectra were recorded using a 60-SXB IR spectrometer. ICP tests were carried out using an Optima 4300DV. XPS measurements were performed using a VG MultiLab 2000 instrument. FESEM images were collected with a JEOL JSM-7100F at an acceleration voltage of 20 kV. TEM, HRTEM, and SAED were performed using a JEOL JEM-2100F STEM/EDS microscope at an accelerating voltage of 200 kV.

**Electrochemical Measurements:** To conduct the electrochemical measurements, 2016 coin cells were assembled in a glove box filled with pure Ar gas. The anode materials were prepared by 70 wt% active materials, 20 wt% acetylene black, and 10 wt% carboxy methyl cellulose (CMC), these materials were mixed with water to produce a slurry, then the slurry was painted on the copper foil and dried at 70 °C overnight. The electrode slices were obtained by cutting the dried foil into a disc and the typical mass loading of the active material was 1.5–3 mg cm<sup>-2</sup>. The lithium metal was used as the counter electrode and the 1 M solution of LiPF<sub>6</sub> in ethylene carbonate (EC), diethyl carbonate (DEC), and ethyl methyl carbonate (EMC) (1:1:1, volume ratio) as the electrolyte. The resulting cells were aged for 12 h to ensure the full attachment of the electrolyte to the electrode. The galvanostatic charge–discharge cycling was performed in the potential range from 0.01 to 3.0 V versus Li<sup>+</sup>/Li with a multichannel battery testing system (LAND CT2001A). EIS and CV were tested with an electrochemical workstation (Autolab PGSTAT302N). The GITT measurements were carried out by applying a current pulse of 0.05 A g<sup>-1</sup> for 10 min and then left on open circuit for 0.5 h.

## Supporting Information

Supporting Information is available from the Wiley Online Library or from the author.

## Acknowledgements

W.R., D.L., and C.S. contributed equally to this work. This work was supported by the National Natural Science Fund for Distinguished Young Scholars (51425204), the National Natural Science Foundation of China (51521001), the National Key Research and Development Program of China (2016YFA0202603), the Programme of Introducing Talents of Discipline to Universities (B17034), the Yellow Crane Talent (Science and Technology) Program of Wuhan City, and the Fundamental Research Funds for the Central Universities (WUT: 2016111001, 20171VA100, 20171VA096, 2017111009, and 2017111040).

## Conflict of Interest

The authors declare no conflict of interest.

## Keywords

Fe<sub>2</sub>O<sub>3</sub>/Mn<sub>2</sub>O<sub>3</sub>, heterostructures, lithium-ion battery anodes, nonhierarchical

Received: February 16, 2018

Revised: March 21, 2018

Published online: May 28, 2018

- [1] a) N. Liu, Z. Lu, J. Zhao, M. T. McDowell, H. W. Lee, W. Zhao, Y. Cui, *Nat. Nanotechnol.* **2014**, *9*, 187; b) J. W. Choi, D. Aurbach, *Nat. Rev. Mater.* **2016**, *1*, 16013; c) L. Mai, M. Yan, Y. Zhao, *Nature* **2017**, *546*, 469; d) W. Ren, Z. Zhu, Q. An, L. Mai, *Small* **2017**, *13*, 1604181.
- [2] a) Y. Wang, X. Yu, S. Xu, J. Bai, R. Xiao, Y. S. Hu, H. Li, X. Q. Yang, L. Chen, X. Huang, *Nat. Commun.* **2013**, *4*, 2365; b) J. Wang, H. Tang, L. Zhang, H. Ren, R. Yu, Q. Jin, J. Qi, D. Mao, M. Yang, Y. Wang, *Nat. Energy* **2016**, *1*, 16050; c) Y. Zhao, X. Li, B. Yan, D. Xiong, D. Li, S. Lawes, X. Sun, *Adv. Energy Mater.* **2016**, *6*, 1502175.
- [3] a) K. Zhao, M. Wen, Y. Dong, L. Zhang, M. Yan, W. Xu, C. Niu, L. Zhou, Q. Wei, W. Ren, X. Wang, L. Mai, *Adv. Energy Mater.* **2017**, *7*, 1601582; b) H. Jiang, Y. Hu, S. Guo, C. Yan, P. S. Lee, C. Li, *ACS Nano* **2014**, *8*, 6038; c) Y. Zhao, J. Feng, X. Liu, F. Wang, L. Wang, C. Shi, L. Huang, X. Feng, X. Chen, L. Xu, *Nat. Commun.* **2014**, *5*, 4565.
- [4] a) K. S. Novoselov, A. Mishchenko, A. Carvalho, A. H. Castro Neto, *Science* **2016**, *353*, aac9439; b) Y. Gong, S. Lei, G. Ye, B. Li, Y. He, K. Keyshar, X. Zhang, Q. Wang, J. Lou, Z. Liu, *Nano Lett.* **2015**, *15*, 6135; c) M. Yue, C. Fang, B. Ding, G. Ji, J. Lee, *Adv. Mater.* **2013**, *25*, 4646.
- [5] L. Mai, F. Yang, Y. Zhao, X. Xu, L. Xu, Y. Luo, *Nat. Commun.* **2011**, *2*, 381.
- [6] G. Gu, L. Chen, Z. Ju, H. Xu, J. Yang, Y. Qian, *Adv. Funct. Mater.* **2013**, *23*, 4049.
- [7] a) D. J. Milliron, S. M. Hughes, Y. Cui, L. Manna, J. Li, L. W. Wang, A. P. Alivisatos, *Nature* **2004**, *430*, 190; b) M. Lin, G. H. Kim, J. H. Kim, J. W. Oh, J. M. Nam, *J. Am. Chem. Soc.* **2017**, *139*, 10180.
- [8] P. C. Chen, X. Liu, J. L. Hedrick, Z. Xie, S. Wang, Q. Y. Lin, M. C. Hersam, V. P. Dravid, C. A. Mirkin, *Science* **2016**, *352*, 1565.
- [9] a) Z. Wang, L. Zhou, X. W. Lou, *Adv. Mater.* **2012**, *24*, 1903; b) L. Shen, L. Yu, X. Y. Yu, X. Zhang, X. W. Lou, *Angew. Chem.* **2015**, *54*, 1868; c) S. Xu, C. M. Hessel, H. Ren, R. Yu, Q. Jin, M. Yang, H. Zhao, D. Wang, *Energy Environ. Sci.* **2014**, *7*, 632; d) H. Sun, G. Xin, T. Hu, M. Yu, D. Shao, X. Sun, J. Lian, *Nat. Commun.* **2014**, *5*, 4526; e) H. Liu, W. Li, D. Shen, D. Zhao, G. Wang, *J. Am. Chem. Soc.* **2015**, *137*, 13161.



- [10] a) W. J. Yu, L. Zhang, P. X. Hou, F. Li, C. Liu, H. M. Cheng, *Adv. Energy Mater.* **2016**, *6*, 1501755; b) K. Cao, H. Liu, X. Xu, Y. Wang, L. Jiao, *Chem. Commun.* **2016**, *6*, 11414.
- [11] a) A. G. Nasibulin, S. Rackauskas, H. Jiang, Y. Tian, P. R. Mudimela, S. D. Shandakov, L. I. Nasibulina, S. Jani, E. I. Kauppinen, *Nano Res.* **2010**, *2*, 373; b) A. M. Jubb, H. C. Allen, *ACS Appl. Mater. Interfaces* **2010**, *2*, 2804.
- [12] a) Y. F. Han, K. Ramesh, L. Chen, E. Widjaja, A. S. Chilukoti, F. Chen, *J. Phys. Chem. C* **2007**, *111*, 2830; b) Y. F. Han, F. Chen, Z. Zhong, K. Ramesh, A. L. Chen, E. Widjaja, *J. Phys. Chem. B* **2006**, *110*, 24450.
- [13] a) K. Sultan, M. Ikram, K. Asokan, *RSC Adv.* **2015**, *5*, 93867; b) L. Yang, A. Zhang, Y. Dai, X. Wu, *J. Mater. Sci.: Mater. Electron.* **2017**, *28*, 8872.
- [14] a) K. Woo, H. J. Lee, J.-P. Ahn, Y. S. Park, *Adv. Mater.* **2010**, *15*, 1761; b) H. Cao, X. Wu, G. Wang, J. Yin, G. Yin, F. Zhang, J. Liu, *J. Phys. Chem. C* **2012**, *116*, 21109.
- [15] a) Y. Qiu, G. L. Xu, K. Yan, H. Sun, J. Xiao, S. Yang, S. G. Sun, L. Jin, H. Deng, *J. Mater. Chem.* **2011**, *21*, 6346; b) Y. Yang, Y. Liu, K. Pu, X. Chen, H. Tian, M. Gao, M. Zhu, H. Pan, *Adv. Funct. Mater.* **2017**, *27*, 1605011.
- [16] O. B. Chae, J. Kim, I. Park, H. Jeong, J. H. Ku, H. R. Ji, K. Kang, S. M. Oh, *Chem. Mater.* **2014**, *26*, 5874.
- [17] V. Augustyn, J. Come, M. A. Lowe, J. W. Kim, P. L. Taberna, S. H. Tolbert, H. D. Abruña, P. Simon, B. Dunn, *Nat. Mater.* **2013**, *12*, 518.
- [18] a) Y. Xu, Y. Zhu, Y. Liu, C. Wang, *Adv. Energy Mater.* **2013**, *3*, 128; b) S. Lee, Y. Cho, H. K. Song, K. T. Lee, J. Cho, *Angew. Chem.* **2012**, *51*, 8748.
- [19] a) Y. You, H. R. Yao, S. Xin, Y. X. Yin, T. T. Zuo, C. P. Yang, Y. G. Guo, Y. Cui, L. J. Wan, J. B. Goodenough, *Adv. Mater.* **2016**, *28*, 7243; b) W. Ren, M. Qin, Z. Zhu, M. Yan, Q. Li, L. Zhang, D. Liu, L. Mai, *Nano Lett.* **2017**, *17*, 4713.